Supporting Information

Methods

1. Focused ultrasound system and acoustic characterization

The FUS system that was designed and built in house is composed of an air-backed spherically curved transducer (frequency: 1.025 MHz; diameter/radius of curvature: 4/3 cm) that is attached to a water filled 3D printed cone with an exit window made of thin Mylar membrane (**Fig. 1A**). The system is mounted on a 3D positioning system and target localization in X-Y directions (left/right, superior/inferior) is performed with needle guidance (**Fig. 1A**).

The FUS transducer spatial profile was modeled using the Field II program (**Fig. S1**). The experimental spatial characterization of the FUS was performed with a 0.2 mm hydrophone (ONDA, HNC-0200, Sunnyvale, CA, USA) that was attached to a motor-driven 3D scanning system (Velmex, 3 axis UniSlide System MSU2004, Bloomfield, NY, USA). We also measured the efficiency of the transducer, by comparing the electrical power input to the FUS, which was measured with an RF power meter (Agilent, E4419B RF Power Meter, Santa Clara, CA 95051USA) to the acoustic power output, which was determined with the radiation force balance method using a digital balance (Mettler-Toledo, Dual Range XS205, Columbus, OH, USA). The FUS transducer was 56% efficient.

Ultrasound gel and plastic cranial windows ensured good acoustic coupling with the targeted region (< 5% inertial losses). The -6dB transverse and axial focal region of the FUS system is 2 mm and 9 mm respectively.

2. Experimental protocol.

All animal procedures were performed according to the guidelines of the Public Health Policy on the Humane Care of Laboratory Animals and approved by the Institutional Animal Care and Use Committee of Massachusetts General Hospital. Human *HER2*-amplified and estrogen dependent BT474 breast cancer cells that were genetically modified to express green fluorescent protein were stereotactically implanted in the brain of mice with cranial windows, as previously described (1, 2). After cell implantation, tumor growth was monitored using Gluc measurements, as described before (3). When tumors reached a size of ~20-40 mm^3, we performed BTB disruption using FUS exposures (10 msec bursts, every 1 sec for 2 min) and concurrent i.v. administration of

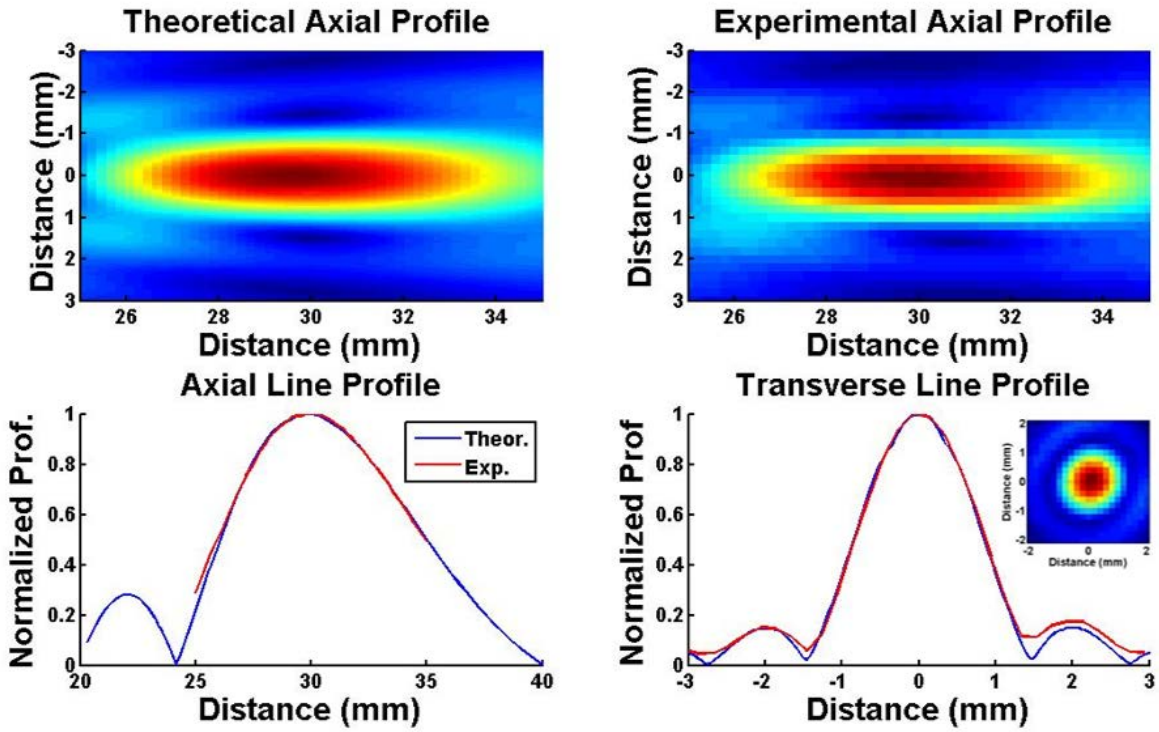

Fig. S1. Comparison of model predications with experimental profiles of the focused ultrasound system.

microbubbles (20 µl/kg, Definity, Lantheus Medical Imaging) **(Fig. 1B)**. A 480 kPa peak negative pressure (based on absolute characterization of the FUS system was used throughout the present study. To cover the entire tumor and its periphery we performed four non-overlapping sonications (X-Y directions).

Shortly after sonication, the pharmacokinetics and intratumoral uptake and clearance of the auto-fluorescent chemotherapeutic agent doxorubicin was measured for 20 minutes using intravital multiphoton microscopy (4). Briefly, the animals were anesthetized and their heads were immobilized on a motorized x-y stage (H101A ProScan II, Prior Scientic) and the tumor margin was localized by intravital multiphoton microscopy. One area of interest was defined for sequential imaging of doxorubicin uptake, based on local vessel architecture and presence of tumor cells. Prior to injection of doxorubicin, one z-stack image was acquired at intervals of 1.38µm, spanning a depth of 100-200 µm. One plane in the vicinity of 50% depth of the z-stack image was chosen and used for subsequent X-Y serial imaging. Three to four sequential images were acquired at 20 sec intervals before intravenous injection of 150µl doxorubicin at a concentration of 7 mg/ml over 30 sec (7.5 mg/kg). Following administration of doxorubicin, continuous sequential image acquisition at 20 sec intervals was continued for a total of 40-50 X-Y images. 8 animals were used in total (#4 FUS-treated and #4 non-FUS treated). For consistency in the notation of the experiments/modeling, Cv is the doxorubicin intensity/concentration in the vessel, Ce is the doxorubicin intensity/concentration in the extracellular/interstitial space, and Ci is the doxorubicin intensity/concentration that has been internalized in the cells.

In separate experiments the antibody-drug conjugate ado-trastuzumab emtansine (T-DM1) (5 mg/kg) was administered i.v. immediately after the sonications. The animals were sacrificed at 4 hours or at 5 days post treatment and the intratumoral distribution of T-DM1 in the brain tumors was determined through tissue staining for human IgG and quantification of fluorescence, as previously described (1).

3. Image analysis.

To analyze the data from the intravital imaging, small image motion artifacts were corrected using the image registration function “imregtform” Matlab (Matlab2016b, Mathworks, Natick, MA) that had as input the local vessel architecture. After registration the vessels were segmented using semiautomatic thresholding of the doxorubicin images, which used as vessel marker, and the doxorubicin kinetics were determined in a 20 x 20 pixel region of interest (ROI) in the vessel and interstitial space (**Fig. 2A**). The drug penetration measurement of doxorubicin was performed by determining the drug profile perpendicular to the vessel using maximum intensity projection across the series of images. The doxorubicin intracellular kinetics were determined on segmented cells. Cell segmentation was performed using the “roipoly” function of Matlab from the thresholded images.

Brains were collected and fixed at the specified time points post-T-DM1 injection (4 hours and 5 days), then embedded in OCT and frozen. Tissues were sectioned (10 µM) and immunostained for CD31 (Millipore, MAB1398Z, mouse mAb, 1:200) and human IgG (Invitrogen, Cat# A-21091, 1:100) as previously described(1). Stained and mounted tissues were imaged on a fluorescent slide scanner (TissueFAXS, Ragon Institute of MGH, MIT, and Harvard) using a 20 x objective (pixel:micron ratio = 0.5). Penetration distance of T-DM1 from vessels was characterized as previously described (1). Area fraction of T-DM1 was quantified using ImageJ software.

4. Single cell doxorubicin kinetics analysis

Magnified images of doxorubicin uptake by endothelial cells (EC) in a brain tumor after FUS-BBB/BTB disruption is shown in **Fig. S2.**

5. Overview of mathematical models for drug transport.

Our mathematical modeling framework simulates the convective and diffusive transport of anticancer agents through the blood stream and across the endothelium into the interstitial space of a tumor along with their uptake by tumor cells. To quantify different tumor micro-environmental drug transport parameters (e.g. BTB diffusion coefficient, vessel wall effective porosity, etc.), we use a simplified tumor cord geometry and experiment-specific parameter-fitting procedures based on the experimentally determined interstitial drug PK of the two different therapeutic agents. The choice of a tumor cord geometry allows us to keep the multidimensional fitting procedures computationally tractable. Then, to study the influence of the spatial structural heterogeneity

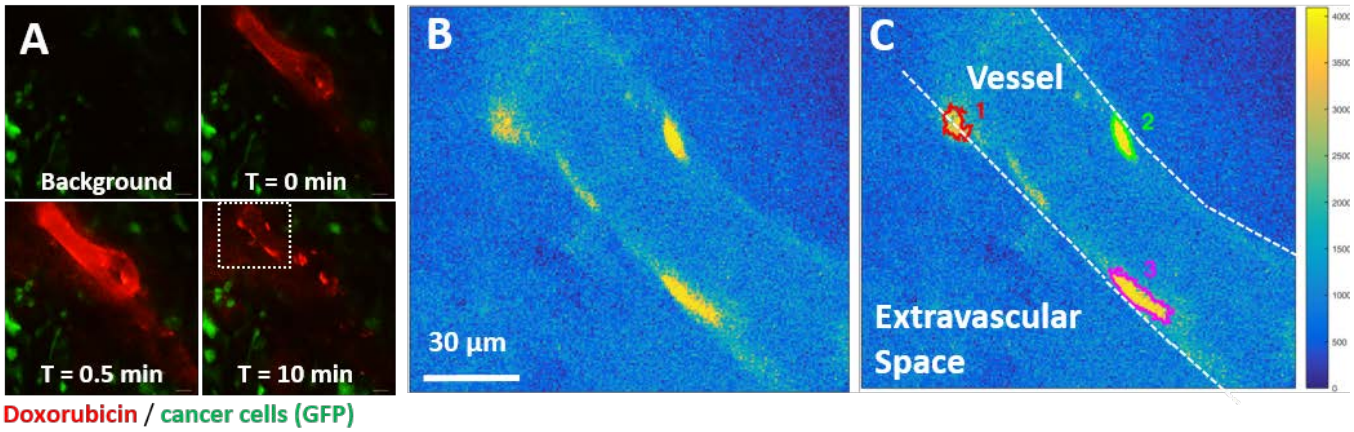

Fig. S2. Doxorubicin uptake by endothelial cells (EC) in a brain tumor after FUS-BBB/BTB disruption. A) Representative sequential images from intravital multiphoton microscopy of doxorubicin in the breast cancer BM model after FUS-BTB disruption. Red: doxorubicin autofluorescence; green: GFP-positive BT474-Gluc cancer cells. B) Magnified image to demonstrate uptake by three segmented endothelial cells. C) Segmented endothelial cells and vessel wall. Color scale shows significant doxorubicin retention by the endothelial cells.

(e.g. vascularity) of the brain tumor microenvironment on the interstitial drug transport after FUS-BTB disruption, we reformulated our model using a vascular network geometry and the previously fitted model parameters.

For the tumor cord geometry model, the computational domain include luminal, vascular wall and interstitial subdomains (**Fig. 4B**). A formal description of the model along with a detailed discussion of the initial and boundary conditions considered are provided below (**SI methods, Section 6**). The geometry of vascular network model is generated based on a previously validated percolation method to mimic the tumor-like vascular structure (**Fig.5A**) (5). A formal description of the model along with a detailed discussion of the initial and boundary conditions considered are provided below (**SI methods, Section 7**).

6. 2D tumor cord model for doxorubicin and T-DM1 interstitial pharmacokinetics

In this section, we describe the details of the Physiologically Based Pharmacokinetic (PBPK) model using 2D tumor cord model. The main processes to be described are the diffusive and convective transport of the agents through the blood stream and across the endothelium into the interstitial space along with their uptake by tumor cells. **Table S2** provides a list of notations used in this work. The computational domain, which is based on the two-dimensional planar model, includes luminal, vascular wall and interstitial subdomains (**Fig. S3**). The luminal domain, with one inlet and one outlet, has a diameter of 30µm, and the vessel wall thickness is 5µm (6). The whole domain is discretized using triangular elements with an average mesh edge length of 3µm that is refined around the vascular wall (mesh edge length 1µm along the vascular wall).

For the flow problem, we assume blood and interstitial fluid to be homogeneous, Newtonian, and incompressible fluids with constant viscosity, µ. Inside the vessel, flow is modeled with the Stokes equation. The flow through vascular wall and interstitial space, which is modeled as isotropic porous medium (with porosity ε_v and ε_i respectively), is described by the Brinkman equation (with a characteristic hydraulic conductivity K). This approach was selected as it provides more flexibility in defining the boundary conditions, as compared to Darcy's law (7). Boundary conditions are as follow: constant velocity, V_{rbc}, at the inlet, a reference pressure at the luminal outlet of 5 mmHg, no-slip velocity at the solid interfaces of the vascular wall subdomain, and a pressure of 1 mmHg at the interstitial outlets,

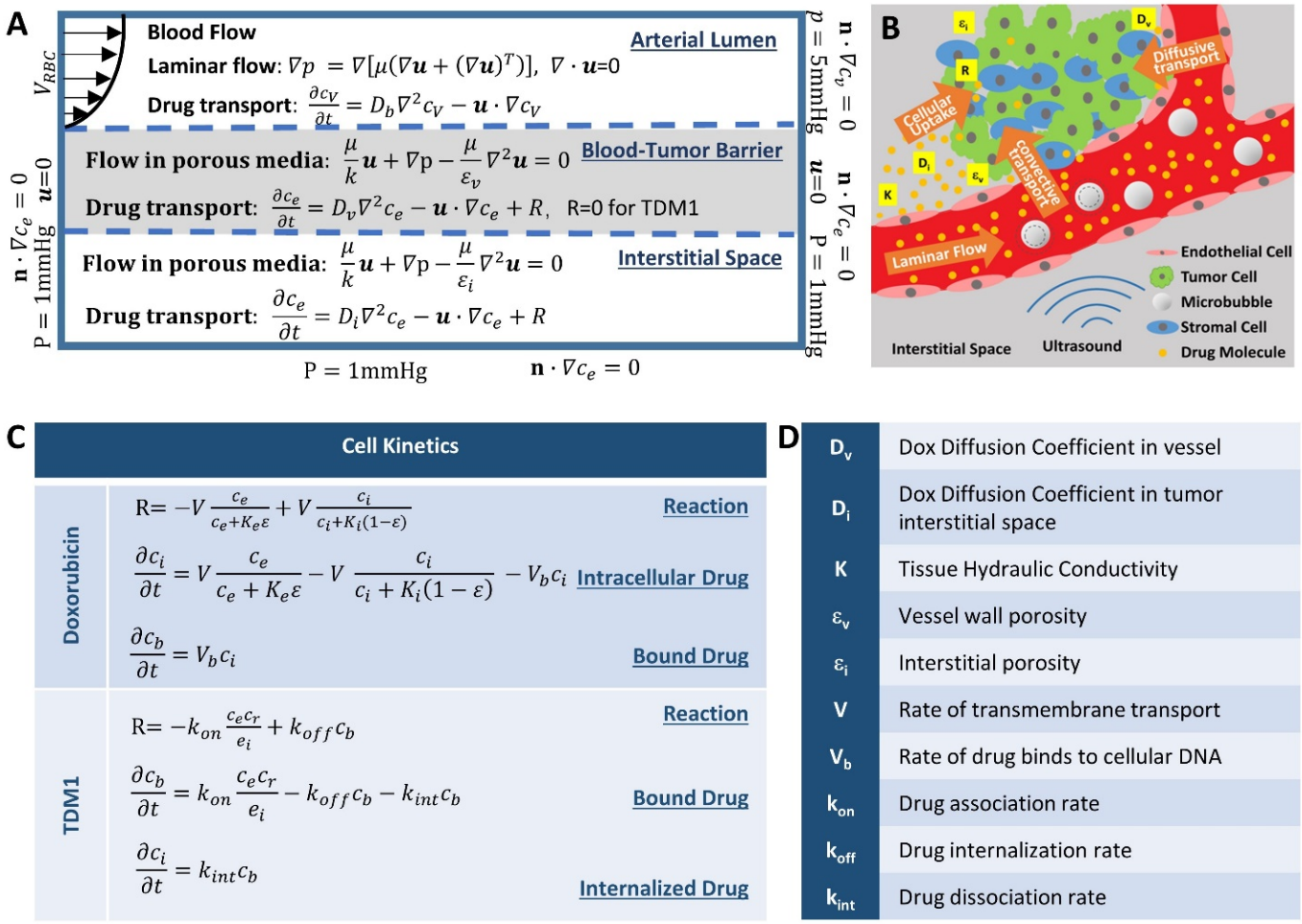

Fig. S3. Mathematical model for doxorubicin and T-DM1 interstitial pharmacokinetics. A) A summary of governing equations and boundary conditions used in the specific subdomain in the mathematical model. B) Schematic illustration of the processes included in the model. C) Mathematical model formulation for cell kinetics of doxorubicin and T-DM1. D) A notation table with transport parameters.

where V_{rbc} is a model parameter (**Table S3**). Continuity of the pressure and velocity fields is enforced across the subdomain boundaries. V_{rbc} was experimentally measured via particle velocimetry of fluorescently labeled red blood cells (8).

For the anticancer agent transport problem, we define the extracellular concentration of any agent as a continuous scalar field, C_e, relative to a peak concentration in the bloodstream inside the vessel. The agent undergoes convection (based on the previously described flow problem), diffusion, and cellular uptake in the interstitial space. This process is modeled as a convection-diffusion problem in the luminal and vascular wall subdomains with diffusion coefficients D_b and D_v, and a reaction-convection-diffusion problem in the interstitial subdomain with diffusion coefficient D_i and an agent-specific reaction term. Boundary concentrations profiles at the luminal inlet, which are experimentally measured drug concentration profiles for doxorubicin (**Fig. 2B**) and constant for T-DM1, and outflow (Neumann boundary conditions) at the rest of boundaries of the computational domain.

The model accounts for the doxorubicin and T-DM1 cellular uptake in the vascular wall and interstitium (reaction term in the reaction-convection-diffusion) as follows. For doxorubicin, cellular uptake in the vascular wall and interstitial space is assumed to undergo reversible cellular uptake (9) and a non-reversible intracellular drug binding to the cell nucleus (extension to the classical model to account for the binding of doxorubicin to DNA), which define two scalar fields for the intracellular concentration, C_i, and bound concentration, C_b, respectively (**Fig. S3**). The reversible drug uptake is modeled based on

Michaelis-Menten kinetics for a given maximum binding rate, porosity, and Michaelis-Menten kinetics constant (9, 10). The agent binds to the nucleus at a constant rate. The T-DM1 kinetics account for agent binding/unbinding to cancer cells/matrix and non-reversible internalization into cancer cells in the interstitial space only given constant binding, unbinding, and internalization rates and tissue porosity (6, 10, 11), which define two additional scalar fields for the bound and internalized concentrations, C_b and C_i, respectively. A summary of the model governing equations, along with the specific subdomains they are applied to, and the imposed boundary conditions are provided in **Fig. S3**.

The parameters of the mathematical model were fitted to the experimental data using a numerical optimization procedure based on an agent-specific objective function and initial values for the model parameters taken from the literature, see **Table S3** and **S4** for doxorubicin and T-DM1, respectively. For doxorubicin, we defined the objective function as the L2-norm of the difference between the experimentally measured pharmacokinetics at a given experiment-specific distance from the vessel wall and the output of the model at the same distance. The experimentally measured doxorubicin pharmacokinetics and equivalent mathematical model output are shown in **Fig. 4B**. Due to the unavailability of experimentally measured T-DM1 pharmacokinetic measurements, we devised a procedure to recover T-DM1 pharmacokinetics in the interstitium based on the experimentally determined T-DM1 penetration data.

We assumed that T-DM1 fluorescence is detectable for relative concentrations above 0.05. This gives us a bound concentration value for any given penetration distance. We then assumed that the concentration goes from 0 to 0.05 over a period of 4 hours and that the dynamics are governed by the analytic solution of a one-dimensional advection-diffusion problem where the TDM1 concentration is given for a distance *x* from the vessel and time *t*:

$$C_b(x,t) = \frac{C_0}{2}\mathrm{erfc}\left(\frac{x-ut}{\sqrt{4D_x t}}\right), \qquad [\mathbf{S1}]$$

where C_0=0.05, u is the interstitial flow velocity obtained from the matching doxorubicin model (non-FUS vs FUS), D_x=4×10^{-2} μm^2/s is a reference diffusion value, and *erfc* is the complementary error function. The T-DM1 profiles based on equation [1] for control (no-FUS) and FUS treated along a schematic of the experimental methodology described above are shown in **Fig. 4B**.

This model fit procedure was performed for each set of experimental data available, *i.e.* four repetitions of each experiment class (doxorubicin in non-FUS, doxorubicin after FUS, T-DM1 in non-FUS, T-DM1 after FUS). Statistics in **Table 1, Table 2,** and **Fig. 4** are computed over these repetitions.

The model considers that BTB disruption occurs immediately after the ultrasound exposure (sonication) and remains open for 4 hours after the sonications (12–17). Molecular weight dependent closing of the barrier was not included in 2D tumor cord modeled, as it is expected to have a marginal impact on doxorubicin due to its fast clearance (10 min), whereas in T-DM1 the interstitial drug distribution was measured at 4 hours, hence effective values were used. Systemic agent clearance from the blood plasma and antibody degradation in the tumor tissue were ignored in the current model.

7. Vasculature network model for doxorubicin and T-DM1 interstitial pharmacokinetics

To study the impact of tumor heterogeneity in interstitial transport, we expanded the 2D tumor cord model to a two-dimensional vascular network based model. The vascular network with one inlet and five outlets is generated using the previously validated percolation method for the generation of synthetic tumor-like vascular networks (18), shown in **Fig. 5A**. The computational domain consists of two subdomains, vasculature (average diameter 15 μm) and interstitial space. The whole domain is discretized using triangular elements with an average mesh edge length of 3μm. The mesh is refined around the vascular wall (average mesh edge length 0.8μm along the vascular wall). Inside the vessel, blood flow is modeled following the approach employed in the 2D tumor cord model. Transvascular fluid transport is modeled using Starling's law and assuming no osmotic pressure difference (6). The rate of transvascular fluid flow is defined as:

$$J_f = L_p(P_v - P_i), \qquad [\mathbf{S2}]$$

where $L_p = \frac{\varepsilon_v {r_0}^2}{8\mu d}$ is the hydraulic conductivity of the vessel wall, P_v and P_i are vascular and interstitial pressure respectively, ε_v is the void fraction at vessel wall, r_0 is the pore radius and *d* is the vessel wall thickness. The flow inside interstitial space is modeled with Darcy's Law. For boundary conditions, we define a constant pressure of 25 mmHg at the inlet and 5 mmHg at the luminal outlet, and zero pressure at the interstitial outlets (19).

The anticancer agent transport in the luminal subdomain is modeled as a convection-diffusion problem, and a reaction-convection-diffusion problem in the interstitial subdomain, as described for the 2D tumor cord model. For transvascular anticancer agent transport, we first calculate the Péclet number across the vessel wall

$$P_e = \frac{L_p(P_v - P_i)(1-\sigma_f)}{P}, \qquad [\mathbf{S3}]$$

where σ_f is the reflection coefficient and P is the vascular diffusive permeability,

$$\sigma_f = 1 - W,\ P = \frac{HD_v}{d}, \qquad [\mathbf{S4}]$$

and H and W are the diffusive and convective hindrance factors that depend on the relative size of the particles to the pores (20).

$$H = \varphi(1 - 2.1044\alpha + 2.089\alpha^3 - 0.948\alpha^5), \qquad [\mathbf{S5}]$$

$$W = \varphi(2-\varphi)\left(1 - \frac{2}{3}\alpha^2 - 0.163\alpha^3\right), \qquad [\mathbf{S6}]$$

where α is the particle size to pore size ratio and $\varphi = (1-\alpha)^2$.

The rate of drug transvascular transport J_s across the vessel wall is modeled using Starling's approximation (6, 20). When the Péclet number is less than or equal to 1, the Kedem-Katchalsky equation is used

$$J_s = J_f(1-\sigma_f)\frac{\Delta C}{\ln(C_v/C_e)} + \Delta C, \qquad [\mathbf{S7}]$$

where ΔC is the anticancer agent concentration difference across the vessel wall. When the Péclet number is greater than 1, the Patlak equation is used

$$J_s = J_f(1-\sigma_f)\frac{C_v e^{Pe} - C_e}{e^{Pe} - 1}, \qquad [\mathbf{S8}]$$

For boundary condition, we use agent-specific concentrations profiles at the luminal inlet as described before, outflow (Neumann boundary condition) at the luminal outlet and the concentration at the rest of the boundary is set to be zero.

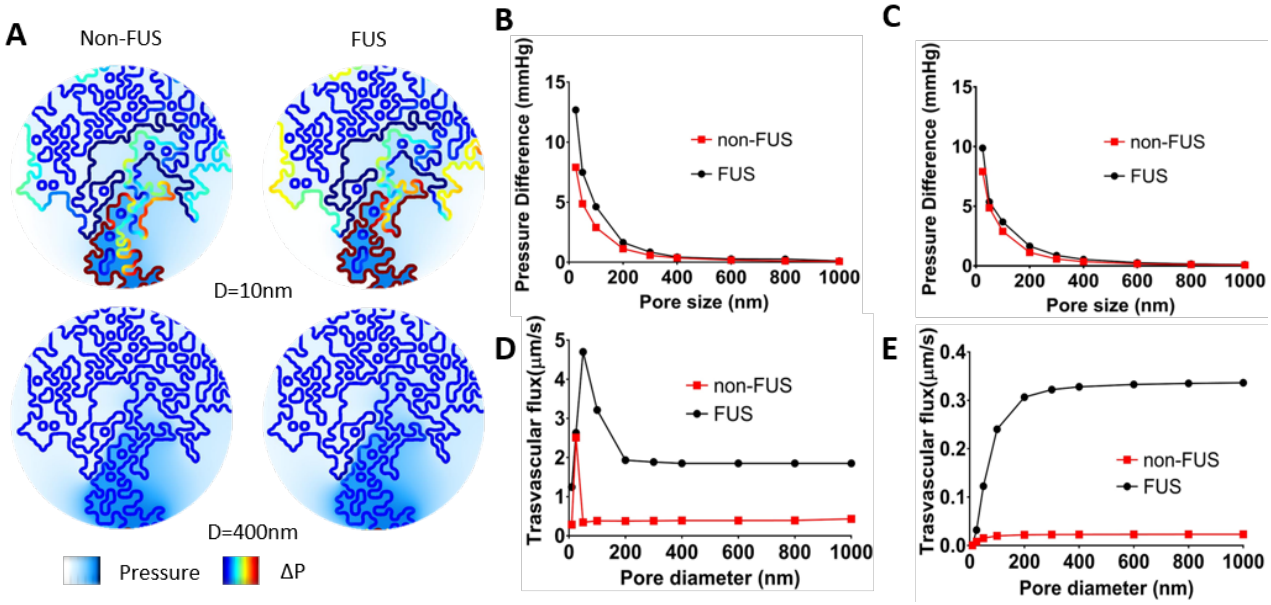

Fig. S4. Pressure distribution and transvascular pressure difference with varies pore sizes. A) Qualitative demonstration of pressure field and transvascular pressure difference for doxorubicin with pore diameter of 10m and 400nm. Quantification of transvascular pressure difference as a function of vessel wall pore diameter for the percolation model B) Doxorubicin C) T-DM1. Quantification of drug transvascular flux as a function of vessel wall pore diameter D) Doxorubicin E) T-DM1

In addition, in the case that FUS is applied, to model the blood brain barrier closure, we incorporate an exponential decay for porosity ε_v for both agents and vessel wall diffusive coefficient D_v for doxorubicin to baseline value

$$\varepsilon_v = C_{\varepsilon_v} e^{-Rt} + B_{\varepsilon_v}, \qquad [\mathbf{S9}]$$
$$D_v = C_{D_v} e^{-Rt} + B_{D_v}, \qquad [\mathbf{S10}]$$

where R is the constant that describes the rate of exponential decay, which is extracted from the decay of measured MRI contrast agent transfer coefficient reported by Park, et al (21). B_{ε_v, D_v} are the baseline value that we fitted with the control experiments using the 2D tumor cord model. C_{ε_v, D_v} are the values that we fitted using the FUS experiments.

To study influence of vascular pore size on transvascular transport, we performed simulations using vascular network based model with an average of previously fitted transport parameters (**Table 1 and 2**). The transvascular drug transport is defined as transvascular mass flux normalized by the average transvascular concentration difference and it is calculated at a certain region of interest in the vascular network (19) (**Fig. 5B**). **Fig. S4. A** indicates an elevated interstitial fluid pressure after FUS-BBB/BTB disruption and a transvascular pressure difference drop as pore diameter increases for doxorubicin. **Fig. S4. B-E** shows the transvascular pressure difference and drug transvascular flux for the two different agents as a function of pore diameter. Both pressure difference across the vessel wall and drug transvascular flux are higher after FUS-BBB/BTB disruption as compared to control group (non-FUS). Then we conducted sensitivity analysis to study the relative importance of the different transport parameters and intracellular drug kinetics using different administration protocols with the experiment-specific and drug-specific (fitted) model parameters (**Fig. 5C, Table 1 and 2**). Other parameters used in the vascular network model is shown in **Table S5**.

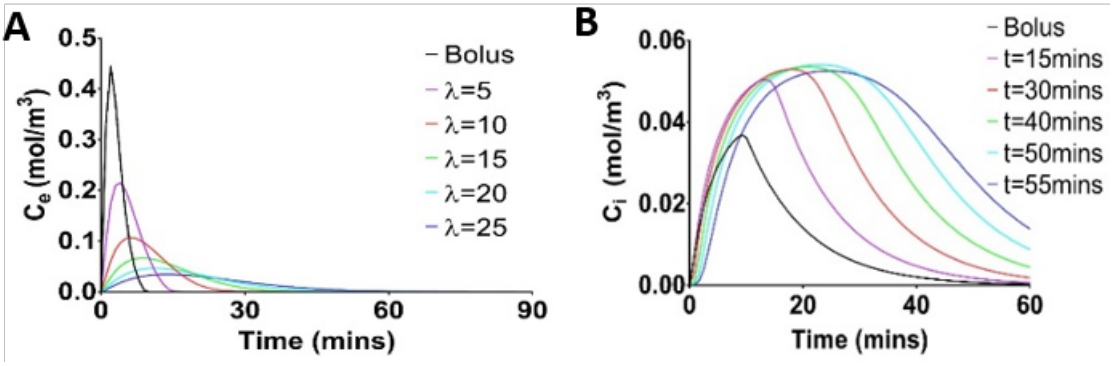

Fig. S5. A) Simulated doxorubicin administration using the Weibull probably distribution function. B) Intracellular drug kinetics for bolus vs infusion administration

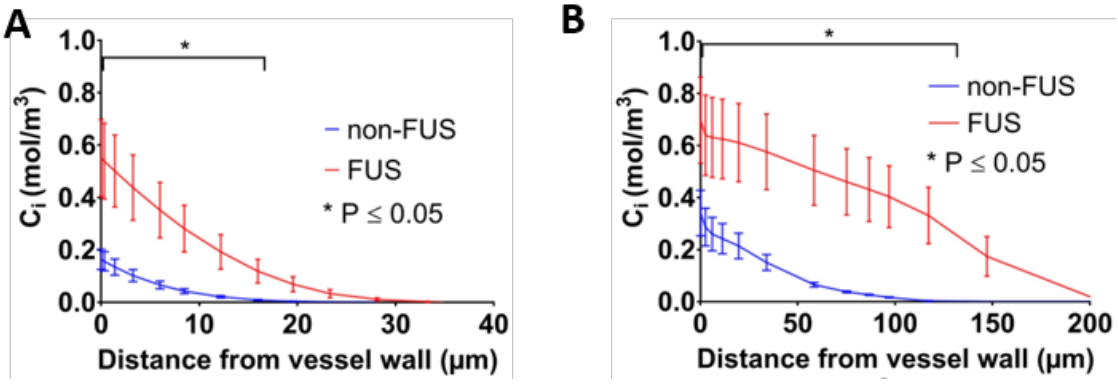

Fig. S6. A**)** T-DM1 intracellular drug kinetics for different at low (left) and high (right) perfusion regions in the percolation model. B) T-DM1 intracellular drug kinetics 10 fold higher dose.

8. Modeling doxorubicin administration protocol

The bolus administration experimental data were fitted using the analytical form of the Weibull probably distribution function (PDF)

$$f(x) = \frac{kC}{\lambda}\left(\frac{x}{\lambda}\right)^{k-1} e^{-\left(\frac{x}{\lambda}\right)^{k}}, \qquad [\mathbf{S11}]$$

Varying the different parameters, C, λ, and k, allowed us to control independently the shape and the scale of the vascular drug concentration profile, while warranting a constant dose (area under the curve) as we move from bolus to infusion. Good fitting with the experimental values was obtain for C=2.72, λ=2, and k=1.4. By varying λ different drug administration protocols can be attained (**Fig. S5A**). These curves were then used as input to the numerical simulations (time-dependent drug concentration profiles at the luminal inlet). **Fig. S5B** shows the intercellular doxorubicin concentration as a function of time for the different administration protocols based on Weibull PDF.

9. Model parameter fit.

The parameters of the mathematical model were fitted using a numerical optimization procedure based on initial reference values taken from the literature (**Table S3 and S4**) and an agent-specific objective function. Sixteen models were fitted comprising four repetitions of each class of experiment: non-FUS vs FUS and doxorubicin vs T-DM1. For doxorubicin, we took advantage of experimentally determined doxorubicin kinetics measured 20 μm from the vessel wall to define the objective function as the difference between this measurement and the output of the model at the same point. To quantify the rate of cellular transmembrane transport from the single cell kinetic measurements of more than one cell type (**Fig. 6**), we redefined the objective function to each cell type in turn and fitted for changes in the rate of cellular transmembrane transport by assuming homogeneous well-mixed cell populations (22). The ratio of the endothelial cell populations was set to be 75% of the total vasculature cell population (23). For T-DM1, we reused the agent-independent model parameters ε_v and ε_i, (fitted values from doxorubicin model), and fit the rest. Due to the unavailability of experimentally measured T-DM1 pharmacokinetic measurements, we devised the procedure described above (**SI methods, Section 6**) to recover T-DM1 pharmacokinetics in the interstitium based on the experimentally determined T-DM1 penetration data.

10. Sensitivity analysis

For both agents, we performed sensitivity analyses for the 16 fitted models (4 per case) in order to compare the sensitivity of each model to changes in each of their parameters as well as differences before and after FUS treatment using vasculature network model. Mathematically, we numerically approximate the derivative of the intracellular agent concentration C_i with respect to any parameter P_i, *i.e.* $\frac{\partial C_i}{\partial P_i}$. To be able to compare the sensitivities to different parameters and also across different experiment classes we employed the following normalized measure of sensitivity $S = \frac{\sigma_i}{\max(C_i)}\frac{\partial C_i}{\partial P_i}$, where σ_i is the standard deviation of P_i across the four repetitions of each experiment class and max(C_i) is the peak intracellular concentration measured. S should be interpreted as the relative change in C_i for a given change of P_i that is equally likely for all i.

11. Numerical implementation

The simulations were performed using the commercial package COMSOL (version 5.2a, Burlington, MA, USA), which uses the finite element method to solve the partial differential equations in the model numerically. The computational domain for the 2D tumor cord model and the percolation model was discretized with an average element size of 3μm, and with the grid being refined near the vessel walls in order to be able to capture a larger gradient. For optimization, we employed the Nelder-Mead method with a maximum number of iterations of 1000. For doxorubicin, duration of the simulation was dictated by its clearance that according to the multiphoton microscopy measurements was approximately 12 mins. For T-DM1, duration of the simulation was dictated by time point of immunostaining (4 hours).

References

1. Askoxylakis V, et al. (2016) Preclinical Efficacy of Ado-trastuzumab Emtansine in the Brain Microenvironment. *JNCI J Natl Cancer Inst* 108(2). doi:10.1093/jnci/djv313.

2. Kodack DP, et al. (2017) The brain microenvironment mediates resistance in luminal breast cancer to PI3K inhibition through HER3 activation. *Sci Transl Med* 9(391):eaal4682.

3. Kodack DP, et al. (2012) Combined targeting of HER2 and VEGFR2 for effective treatment of HER2-amplified breast cancer brain metastases. *Proc Natl Acad Sci* 109(45):E3119–E3127.

4. Askoxylakis V, et al. (2017) A cerebellar window for intravital imaging of normal and disease states in mice. *Nat Protoc* 12(11):2251–2262.

5. Baish JW, et al. (1996) Role of Tumor Vascular Architecture in Nutrient and Drug Delivery: An Invasion Percolation-Based Network Model. *Microvasc Res* 51(3):327–346.

6. Stylianopoulos T, Jain RK (2013) Combining two strategies to improve perfusion and drug delivery in solid tumors. *Proc Natl Acad Sci U S A* 110(46):18632–18637.

7. Stylianopoulos T, Munn LL, Jain RK (2018) Reengineering the Physical Microenvironment of Tumors to Improve Drug Delivery and Efficacy: From Mathematical Modeling to Bench to Bedside. *Trends Cancer* 4(4):292–319.

8. Kamoun WS, et al. (2010) Simultaneous measurement of RBC velocity, flux, hematocrit and shear rate in tumor vascular networks. *Nat Methods* 7(8):655–660.

9. Eikenberry S (2009) A tumor cord model for Doxorubicin delivery and dose optimization in solid tumors. *Theor Biol Med Model* 6:16.

10. Thurber GM, Weissleder R (2011) A Systems Approach for Tumor Pharmacokinetics. *PLOS ONE* 6(9):e24696.

11. Schmidt MM, Wittrup KD (2009) A modeling analysis of the effects of molecular size and binding affinity on tumor targeting. *Mol Cancer Ther* 8(10):2861–2871.

12. Hynynen K, McDannold N, Vykhodtseva N, Jolesz FA (2001) Noninvasive MR Imaging–guided Focal Opening of the Blood-Brain Barrier in Rabbits1. *Radiology* 220(3):640–646.

13. Sheikov N, et al. (2006) Brain arterioles show more active vesicular transport of blood-borne tracer molecules than capillaries and venules after focused ultrasound-evoked opening of the blood-brain barrier. *Ultrasound Med Biol* 32:1399–409.

14. Hynynen K, McDannold N, Sheikov NA, Jolesz FA, Vykhodtseva N (2005) Local and reversible blood-brain barrier disruption by noninvasive focused ultrasound at frequencies suitable for trans-skull sonications. *NeuroImage* 24(1):12–20.

15. Park E-J, Zhang Y-Z, Vykhodtseva N, McDannold N (2012) Ultrasound-mediated blood-brain/blood-tumor barrier disruption improves outcomes with trastuzumab in a breast cancer brain metastasis model. *J Controlled Release* 163(3):277–284.

16. Marty B, et al. (2012) Dynamic Study of Blood–Brain Barrier Closure after its Disruption using Ultrasound: A Quantitative Analysis. *J Cereb Blood Flow Metab* 32(10):1948–1958.

17. Cho EE, Drazic J, Ganguly M, Stefanovic B, Hynynen K (2011) Two-Photon Fluorescence Microscopy Study of Cerebrovascular Dynamics in Ultrasound-Induced Blood—Brain Barrier Opening. *J Cereb Blood Flow Metab* 31(9):1852–1862.

18. Baish JW, et al. (1996) Role of tumor vascular architecture in nutrient and drug delivery: an invasion percolation-based network model. *Microvasc Res* 51(3):327–346.

19. Chauhan VP, et al. (2012) Normalization of tumour blood vessels improves the delivery of nanomedicines in a size-dependent manner. *Nat Nanotechnol* 7(6):383–388.

20. Truskey G, Yuan F, Katz D (2009) Transport Phenomena in Biological Systems. *Pearson Prentice Hall, Upper Saddle River, NJ*, pp 415–439.

21. Park J, Zhang Y, Vykhodtseva N, Jolesz FA, McDannold NJ (2012) The kinetics of blood brain barrier permeability and targeted doxorubicin delivery into brain induced by focused ultrasound. *J Control Release Off J Control Release Soc* 162(1):134–142.

22. Beerenwinkel N, Schwarz RF, Gerstung M, Markowetz F (2015) Cancer Evolution: Mathematical Models and Computational Inference. *Syst Biol* 64(1):e1–e25.

23. Wong AD, et al. (2013) The blood-brain barrier: an engineering perspective. *Front Neuroengineering* 6. doi:10.3389/fneng.2013.00007.

24. Treat LH, et al. (2007) Targeted delivery of doxorubicin to the rat brain at therapeutic levels

using MRI-guided focused ultrasound. *Int J Cancer* 121(4):901–907.

25. Kovacs Z, et al. (2014) Prolonged survival upon ultrasound-enhanced doxorubicin delivery in two syngenic glioblastoma mouse models. *J Controlled Release* 187:74–82.

26. Park J, Aryal M, Vykhodtseva N, Zhang Y-Z, McDannold N (2017) Evaluation of permeability, doxorubicin delivery, and drug retention in a rat brain tumor model after ultrasound-induced blood-tumor barrier disruption. *J Controlled Release* 250:77–85.

27. Carpentier A, et al. (2016) Clinical trial of blood-brain barrier disruption by pulsed ultrasound. *Sci Transl Med* 8(343):343re2-343re2.

28. Liu H-L, et al. (2010) Blood-Brain Barrier Disruption with Focused Ultrasound Enhances Delivery of Chemotherapeutic Drugs for Glioblastoma Treatment. *Radiology* 255(2):415–425.

29. Mei J, et al. (2009) Experimental Study on Targeted Methotrexate Delivery to the Rabbit Brain via Magnetic Resonance Imaging–Guided Focused Ultrasound. *J Ultrasound Med* 28(7):871–880.

30. Wei K-C, et al. (2013) Focused Ultrasound-Induced Blood–Brain Barrier Opening to Enhance Temozolomide Delivery for Glioblastoma Treatment: A Preclinical Study. *PLOS ONE* 8(3):e58995.

31. Liu H-L, et al. (2014) Pharmacodynamic and Therapeutic Investigation of Focused Ultrasound-Induced Blood-Brain Barrier Opening for Enhanced Temozolomide Delivery in Glioma Treatment. *PLOS ONE* 9(12):e114311.

32. Beccaria K, et al. (2015) Ultrasound-induced opening of the blood-brain barrier to enhance temozolomide and irinotecan delivery: an experimental study in rabbits. *J Neurosurg* 124(6):1602–1610.

33. Kinoshita M, McDannold N, Jolesz FA, Hynynen K (2006) Noninvasive localized delivery of Herceptin to the mouse brain by MRI-guided focused ultrasound-induced blood–brain barrier disruption. *Proc Natl Acad Sci* 103(31):11719–11723.

34. Park E-J, Zhang Y-Z, Vykhodtseva N, McDannold N (2012) Ultrasound-mediated blood-brain/blood-tumor barrier disruption improves outcomes with trastuzumab in a breast cancer brain metastasis model. *J Control Release Off J Control Release Soc* 163(3):277–284.

35. Kobus T, Zervantonakis IK, Zhang Y, McDannold NJ (2016) Growth inhibition in a brain metastasis model by antibody delivery using focused ultrasound-mediated blood-brain barrier disruption. *J Control Release Off J Control Release Soc* 238:281–288.

36. Chen P-Y, et al. (2015) Focused ultrasound-induced blood–brain barrier opening to enhance interleukin-12 delivery for brain tumor immunotherapy: a preclinical feasibility study. *J Transl Med* 13. doi:10.1186/s12967-015-0451-y.

37. Liu H-L, et al. (2016) Focused Ultrasound Enhances Central Nervous System Delivery of Bevacizumab for Malignant Glioma Treatment. *Radiology* 281(1):99–108.

38. Alkins RD, Brodersen PM, Sodhi RNS, Hynynen K (2013) Enhancing drug delivery for boron neutron capture therapy of brain tumors with focused ultrasound. *Neuro-Oncol* 15(9):1225–1235.

39. Yang F-Y, et al. (2014) Pharmacokinetics of BPA in Gliomas with Ultrasound Induced Blood-Brain Barrier Disruption as Measured by Microdialysis. *PLOS ONE* 9(6):e100104.

40. Yang F-Y, et al. (2015) Focused ultrasound enhanced molecular imaging and gene therapy for multifusion reporter gene in glioma-bearing rat model. *Oncotarget* 6(34):36260–36268.

41. Chang E-L, et al. (2017) Angiogenesis-targeting microbubbles combined with ultrasound-mediated gene therapy in brain tumors. *J Controlled Release* 255:164–175.

42. Alkins R, et al. (2013) Focused Ultrasound Delivers Targeted Immune Cells to Metastatic Brain Tumors. *Cancer Res* 73(6):1892–1899.

43. Alkins R, Burgess A, Kerbel R, Wels WS, Hynynen K (2016) Early treatment of HER2-amplified brain tumors with targeted NK-92 cells and focused ultrasound improves survival. *Neuro-Oncol* 18(7):974–981.

44. Treat LH, McDannold N, Zhang Y, Vykhodtseva N, Hynynen K (2012) Improved Anti-Tumor Effect of Liposomal Doxorubicin After Targeted Blood-Brain Barrier Disruption by MRI-

Guided Focused Ultrasound in Rat Glioma. *Ultrasound Med Biol* 38(10):1716–1725.

45. Yang F-Y, et al. (2012) Pharmacokinetic Analysis of 111In-Labeled Liposomal Doxorubicin in Murine Glioblastoma after Blood-Brain Barrier Disruption by Focused Ultrasound. *PLOS ONE* 7(9):e45468.

46. Yang F-Y, et al. (2012) Treating glioblastoma multiforme with selective high-dose liposomal doxorubicin chemotherapy induced by repeated focused ultrasound. *Int J Nanomedicine* 7:965–974.

47. Yang F-Y, et al. (2012) Focused ultrasound and interleukin-4 receptor-targeted liposomal doxorubicin for enhanced targeted drug delivery and antitumor effect in glioblastoma multiforme. *J Controlled Release* 160(3):652–658.

48. Aryal M, Vykhodtseva N, Zhang Y-Z, Park J, McDannold N (2013) Multiple treatments with liposomal doxorubicin and ultrasound-induced disruption of blood-tumor and blood-brain barriers improves outcomes in a rat glioma model. *J Control Release Off J Control Release Soc* 169(0):103–111.

49. Aryal M, Vykhodtseva N, Zhang Y-Z, McDannold N (2015) Multiple sessions of liposomal doxorubicin delivery via focused ultrasound mediated blood–brain barrier disruption: A safety study. *J Controlled Release* 204:60–69.

50. Sun T, et al. (2017) Closed-loop control of targeted ultrasound drug delivery across the blood–brain/tumor barriers in a rat glioma model. *Proc Natl Acad Sci* 114(48):E10281–E10290.

51. Timbie KF, et al. (2017) MR image-guided delivery of cisplatin-loaded brain-penetrating nanoparticles to invasive glioma with focused ultrasound. *J Controlled Release* 263:120–131.

52. Shen Y, et al. (2017) Enhanced delivery of paclitaxel liposomes using focused ultrasound with microbubbles for treating nude mice bearing intracranial glioblastoma xenografts. *Int J Nanomedicine* 12:5613–5629.

53. Aryal M, Park J, Vykhodtseva N, Zhang Y-Z, McDannold N (2015) Enhancement in blood-tumor barrier permeability and delivery of liposomal doxorubicin using focused ultrasound and microbubbles: evaluation during tumor progression in a rat glioma model. *Phys Med Biol* 60(6):2511–2527.

54. Zhao Y-Z, et al. (2016) Glioma-targeted therapy using Cilengitide nanoparticles combined with UTMD enhanced delivery. *J Controlled Release* 224:112–125.

55. Diaz RJ, et al. (2014) Focused ultrasound delivery of Raman nanoparticles across the blood-brain barrier: Potential for targeting experimental brain tumors. *Nanomedicine Nanotechnol Biol Med* 10(5):e1075–e1087.

56. Chen Y-C, et al. (2015) Targeting microbubbles-carrying TGFβ1 inhibitor combined with ultrasound sonication induce BBB/BTB disruption to enhance nanomedicine treatment for brain tumors. *J Controlled Release* 211:53–62.

57. Chen P-Y, et al. (2010) Novel magnetic/ultrasound focusing system enhances nanoparticle drug delivery for glioma treatment. *Neuro-Oncol* 12(10):1050–1060.

58. Liu H-L, et al. (2010) Magnetic resonance monitoring of focused ultrasound/magnetic nanoparticle targeting delivery of therapeutic agents to the brain. *Proc Natl Acad Sci U S A* 107(34):15205–15210.

59. Fan C-H, et al. (2016) Ultrasound/Magnetic Targeting with SPIO-DOX-Microbubble Complex for Image-Guided Drug Delivery in Brain Tumors. *Theranostics* 6(10):1542–1556.

60. Ting C-Y, et al. (2012) Concurrent blood–brain barrier opening and local drug delivery using drug-carrying microbubbles and focused ultrasound for brain glioma treatment. *Biomaterials* 33(2):704–712.

61. Fan C-H, et al. (2015) Drug-loaded bubbles with matched focused ultrasound excitation for concurrent blood–brain barrier opening and brain-tumor drug delivery. *Acta Biomater* 15:89–101.

62. Fan C-H, et al. (2013) Antiangiogenic-targeting drug-loaded microbubbles combined with focused ultrasound for glioma treatment. *Biomaterials* 34(8):2142–2155.

63. Fan C-H, et al. (2016) Folate-conjugated gene-carrying microbubbles with focused ultrasound for concurrent blood-brain barrier opening and local gene delivery. *Biomaterials* 106:46–57.

64. Fan C-H, et al. (2013) SPIO-conjugated, doxorubicin-loaded microbubbles for concurrent MRI and focused-ultrasound enhanced brain-tumor drug delivery. *Biomaterials* 34(14):3706–3715.

65. El-Kareh AW, Secomb TW (2000) A Mathematical Model for Comparison of Bolus Injection, Continuous Infusion, and Liposomal Delivery of Doxorubicin to Tumor Cells. *Neoplasia N Y N* 2(4):325–338.

66. Panagiotaki E, et al. (2014) Noninvasive Quantification of Solid Tumor Microstructure Using VERDICT MRI. *Cancer Res* 74(7):1902–1912.

67. Vincensini D, et al. (2007) Magnetic resonance imaging measurements of vascular permeability and extracellular volume fraction of breast tumors by dynamic Gd-DTPA-enhanced relaxometry. *Magn Reson Imaging* 25(3):293–302.

68. Miller MA, et al. (2015) Predicting therapeutic nanoparticle efficacy using a companion MR imaging nanoparticle. *Sci Transl Med* 7(314):314ra183.

69. Swabb EA, Wei J, Gullino PM (1974) Diffusion and Convection in Normal and Neoplastic Tissues. *Cancer Res* 34(10):2814–2822.

70. Wu NZ, Klitzman B, Rosner G, Needham D, Dewhirst MW (1993) Measurement of material extravasation in microvascular networks using fluorescence video-microscopy. *Microvasc Res* 46(2):231–253.

71. Weinberg BD, Patel RB, Exner AA, Saidel GM, Gao J (2007) Modeling doxorubicin transport to improve intratumoral drug delivery to RF ablated tumors. *J Controlled Release* 124(1–2):11–19.

72. Pluen A, et al. (2001) Role of tumor–host interactions in interstitial diffusion of macromolecules: Cranial vs. subcutaneous tumors. *Proc Natl Acad Sci* 98(8):4628–4633.

73. Thurber GM, Weissleder R (2011) A Systems Approach for Tumor Pharmacokinetics. *PLOS ONE* 6(9):e24696.

74. El-Kareh AW, Secomb TW (2000) A Mathematical Model for Comparison of Bolus Injection, Continuous Infusion, and Liposomal Delivery of Doxorubicin to Tumor Cells. *Neoplasia N Y N* 2(4):325–338.

75. Jackson TL (2003) Intracellular Accumulation and Mechanism of Action of Doxorubicin in a Spatio-temporal Tumor Model. *J Theor Biol* 220(2):201–213.

76. Bender B, et al. (2014) A Mechanistic Pharmacokinetic Model Elucidating the Disposition of Trastuzumab Emtansine (T-DM1), an Antibody–Drug Conjugate (ADC) for Treatment of Metastatic Breast Cancer. *AAPS J* 16(5):994–1008.

77. Mok W, Stylianopoulos T, Boucher Y, Jain RK (2009) Mathematical Modeling of Herpes Simplex Virus Distribution in Solid Tumors: Implications for Cancer Gene Therapy. *Clin Cancer Res Off J Am Assoc Cancer Res* 15(7):2352–2360.

78. Jackson TL (2003) Intracellular Accumulation and Mechanism of Action of Doxorubicin in a Spatio-temporal Tumor Model. *J Theor Biol* 220(2):201–213.

79. Gazit Y, Berk DA, Leunig M, Baxter LT, Jain RK (1995) Scale-invariant behavior and vascular network formation in normal and tumor tissue. *Phys Rev Lett* 75(12):2428–2431.

80. Jain RK (1987) Transport of molecules across tumor vasculature. *Cancer Metastasis Rev* 6(4):559–593.

Table S1. Summary of studies reporting the impact of FUS-BBB/BTB disruption on the delivery of anticancer agents in murine in brain tumor models. Data form the first clinical trial have also been included. Note that the delivery of some nanoparticle formulations reported in the literature was magnetically or acoustically actuated.

Tumor model [a]	Therapeutic agent	Size	Imaging of BBB Disruption/ Correlation With Drug Delivery	Quantification of Drug Uptake	Key Finding	Unanswered Questions	Ref
Free Drug							
Healthy Animal (Rat)	Doxorubicin (Chemotherapy)	580 Da	Contrast-enhanced T1-W MRI and Trypan Blue. Modest correlation between MRI signal enhancement and Dox concentration: r^2=0.76.	Fluorometric assay	Parametric study that demonstrated high level of dox extravasation in the brain	Are the findings applicable to brain tumors?	(24)
Healthy Animal (Rat)	Doxorubicin (Chemotherapy)	580 Da	Dynamic Contrast Enhanced MRI. Modest correlation between Dox concentration and K_{trans}: r^2=0.5.	Fluorometric assay	Examined the kinetics of the BBB permeability using DCE-MRI. 1.5-fold higher Dox extravasation in double sonicated brain after FUS.	Are the findings applicable to brain tumors?	(21)
GL261 and SMA-560 glioma model (B6-albino mouse)	Doxorubicin (Chemotherapy)	580 Da	Contrast-enhanced T1-W MRI and Trypan Blue. The correlation was not estimated.	Fluorometric assay and HPLC	4-fold increase in DOX extravasation in GL261 model after FUS (119.70 ± 64.60 vs. 29.66 ± 10.13 ng/ml). Significant improvement in survival (IST median 68.2% vs 0%-Dox alone); marginal differences in SMA-560 model.	Is the increase in extravasation of Dox related to changes in BBB/BTB permeability and/or interstitial transport and/or cell kinetics in the two GBM models used? Did FUS improve Dox penetration?	(25)
9L gliosarcoma model (Rat)	Doxorubicin (Chemotherapy)	580 Da	Dynamic Contrast Enhanced MRI. Modest correlation between K_{trans} and Dox concentration: r^2=0.56.	Fluorometric assay	2-fold increase in the transfer coefficient K_{trans} for Gd-DTPA in tumors.	Is the limited correlation between K_{trans} and Dox uptake related to changes in interstitial transport and/or cell uptake/kinetics?	(26)

Human recurrent glioblastoma (GBM)	Carboplatin (Chemotherapy)		Contrast-enhanced T1-W MRI. The correlation was not estimated.	Indirect via contrast-enhanced T1-weighted MR images	BBB opening in humans with Glioblastoma (after tumor resection).	Did FUS change BBB/BTB permeability, interstitial transport, and/or cell kinetics? Did FUS improve penetration and change drug uptake?	(27)
C6 glioma model (Rat)	BCNU (Chemotherapy)	214 Da	Contrast-enhanced T1-W MRI and Evans Blue. The correlation was not estimated.	HPLC	202% increase in BCNU in the FUS targeted region (drug was not flashed from vessels). Significant improvement in survival (IST median 85.9% vs 16%-BCNU alone).	Is the increase of BCNU in the brain related to changes in BBB/BTB permeability, interstitial transport, and/or cell kinetics for the exposures tested? Did FUS improve drug uptake and penetration?	(28)
Healthy Animal (Rabbit)	Methotrexate (Chemotherapy)	545 Da	Contrast-enhanced T1-W MRI and Evans Blue The correlation was not estimated.	HPLC	10-fold increase in drug extravasation after FUS.	Are the findings applicable to brain tumors?	(29)
9L gliosarcoma mode (Rat)	Temozolomide (TMZ) (Chemotherapy)	194 Da	Contrast-enhanced T1-W MRI and Evans Blue. The correlation was not estimated.	HPLC (body fluids)	CSF/plasma ratio increased from 22.7% to 38.6%. Extended the median survival from 20 to 23 days (IST median 72%).	Is the increase in the CSF/plasma ratio of TMZ related to changes in BBB/BTB permeability and/or interstitial transport and/or cell kinetics? Did FUS improve the TMZ penetration and/or change cell uptake?	(30)
U87 glioma model (Mouse)	Temozolomide (TMZ) (Chemotherapy)	194 Da	Evans Blue (2h post treatment). The correlation was not estimated.	HPLC	2-fold increase (non-significant) in TMZ extravasation after FUS. Small improvement survival at dose of 25mg/kg (IST median 108.6% vs 77.7%).	Did the higher TMZ dose improve the drug penetration and/or cell uptake?	(31)

Healthy Animal (Rabbit)	Temozolomide (TMZ) Camptothecin-11 (CPT-11) (Chemotherapy)	194 Da; 586 Da	Evans Blue. The correlation was not estimated.	HPLC	Significant extravasation in the intracerebral concentration of both TMZ (1.25-fold) and CPT-11 (2.9-fold) after FUS. Pre and post FUS drug administration lead to similar extravasation.	Are the findings applicable to brain tumors?	(32)
Healthy Animal (Rat)	Herceptin (trastuzumab) (Antibody)	148 kDa	Contrast-enhanced T1-W MR and Trypan Blue. Modest correlation between Herceptin concentration and MRI signal change: r^2=0.59.	Immunostaining of human IgG	> 3-fold improvement in extravasation of Herceptin (3,257 ng/g of tissue) after FUS.	Are the findings applicable to brain tumors?	(33)
human HER2-positive BT474 model (Rat)	Herceptin (trastuzumab) (Antibody)	148 kDa	Contrast-enhanced T1-W MRI. The correlation was not estimated.	Indirect via contrast-enhanced T1-Weighted MR images	Significant reduction in mean tumor volume	Did FUS improve trastuzumab uptake and penetration?	(34)
Human HER2-positive MDA-MB-361 model (Rat)	HER2-targeting antibodies (trastuzumab and pertuzumab) (Antibody)	148 kDa	Contrast-enhanced T1-W MRI. The correlation was not estimated.	Indirect via contrast-enhanced T1-weighted MR images	Growth inhibition in combined therapy with few complete responders; Modest improvement in survival.	Did FUS improve trastuzumab and pertuzumab uptake and penetration?	(35)
C6 glioma model (Rat)	Interleukin-12 (IL-12) (Antibody)	75 kDa	Evans Blue. The correlation was not estimated.	ELISA assay	1.5-fold higher IL-12 extravasation after FUS as compared to non-FUS control (632.1 ± 358.2 pg/mg). Improved immune response and survival (IST median 43% vs 24% IL-12 alone).	Is the increase in the IL-12 extravasation related to changes in BBB/BTB permeability and/or interstitial transport? Did FUS improve IL-12 penetration and change cell uptake?	(36)
U87 glioma model (Mouse)	Bevacizumab (Antibody)	150 kDa	Dynamic Contrast Enhanced MRI; PET/micro-CT of	HPLC and PET/micro-CT	~6-fold increase with HPLC and 3.5-fold increase with PET/CT in	Is the limited correlation between K_{trans} and BEV uptake related to	(37)

			radiolabeled gallium 68 (68Ga)- bevacizumab; CD31 immunostaining Modest correlation between K_{trans} and Bevacizumab concentration: r^2=0.6. Good PET signal.	with radiolabeled (^{68}Ga)-	the bevacizumab extravasation after FUS. Significant improvement in survival. (IST median 135.5% vs 48.4% vs Antibody alone).	changes in interstitial transport and/or cell uptake/kinetics? Did FUS improve BEV penetration and change cell uptake?	
9L gliosarcoma model (Rat)	boronophenylalanine-fructose (BPA-f)		Contrast-enhanced T1-W MR, and Imaging Mass spectrometry. The correlation was not estimated.	Mass Spectrometry (Imaging)	The tumor to brain ratio of ^{10}B intensity was 6.7±0.5 after FUS vs 4.1±0.4 in the control group (P <0.01) BPA-f alone.	Is the increase in the tumor to brain ratio of ^{10}B intensity related to changes in BBB/BTB permeability and/or interstitial transport and/or cell kinetics? Did FUS improve BPA-f penetration and change cell uptake?	(38)
F98 glioma model (Rats)	boronophenylalanine-fructose (BPA-f)		N/A	Microdialysis probe in brain and tail vain	3.6-fold increase extravasation of BPA-f after FUS (did not confirm the probe was placed in tumor).	Is the increase in the tumor to brain ratio of ^{10}B intensity related to changes in BBB/BTB permeability and/or interstitial transport and/or cell kinetics? Did FUS improve BPA-f penetration and change cell uptake?	(39)
F98 glioma model (Rats)	Herpes virus gene (HSV1-tk) with Ganciclovir prodrug (GCV)	5.5 MDa (152 kbp)	micro-SPECT/CT of ^{23}I-FIAU. The correlation was not estimated.	Indirect via micro-SPECT/CT of ^{23}I-FIAU	~3-fold increase in specific uptake ratio of ^{23}I-FIAU. Modest but significant reduction in tumor size compared to GCV alone.	Is the increase in the specific uptake ratio of ^{23}I-FIAU related to changes in BBB/BTB permeability and/or interstitial transport and/or cell kinetics? Did FUS improve GCV penetration and change cell uptake?	(40)

C6 glioma model (Rat)	Herpes virus gene (HSV1-tk) with Ganciclovir prodrug (GCV)	5.5 MDa (152 kbp)	Evans Blue (1hr post treatment) and bioluminescence imaging of pLUC transfection. The correlation was not estimated.	ELISA assay	2.3-fold higher transfection when FUS combined with VEGFR2-targeted cationic microbubbles than the direct gene (luciferase) injection group. Significant but modest improvement in survival with the pHSV-TK/GCV+FUS.	Is the higher transfection related to changes in BBB/BTB permeability and/or interstitial transport? Did FUS improve GCV penetration?	(41)
Human HER2-positive MDA-MB-361 model (Rat)	NK-92 cells (Cell Therapy)	~10 μm	Contrast-enhanced T1-W MRI. T2*-weighted MRI of magnetic nanoparticle tagged cells. Histologic quantification of HER2-specific NK-92 cells accumulating at the tumor site.	Direct via histology and T2*-weighted MRI (FUS tissue damage gives similar signal)	Increased accumulation of HER2-specific NK-92 cells	Is FUS mediated endothelial damage or changes in the transport properties of the vessels/ interstitial space responsible for the increased NK-92 cell accumulation?	(42)
Human HER2-positive MDA-MB-361 model (Rat)	NK-92 cells (Cell Therapy)	~10 μm	Contrast-enhanced T1-W MRI. The correlation was not estimated.	Indirect via contrast-enhanced T1-weighted MR images	Improvement in long-term survival in 50% of subjects.	Is FUS mediated endothelial damage or changes in the transport properties of the vessels/ interstitial space responsible for the increased NK-92 cell accumulation?	(43)
Drug Nanoparticle Formulations							
9L gliosarcoma model (Rats)	Liposomal doxorubicin (Doxil) (Chemotherapy)	90 nm	Contrast-enhanced T1-W MRI. The correlation was not estimated.	Indirect via contrast-enhanced T1-weighted MR images	Significant but modest improvement in survival.	Did FUS improve Doxil penetration and Dox cell uptake?	(44)
Human GBM 8401	AP-1 targeted - Liposomal doxorubicin	116± 30 nm	microSPECT of 111In-labeled (AP-1)-conjugated Lipo-Dox.	microSPECT of ^{111}In-labeled (AP-1)-	~2.5-fold improvement in extravasation after FUS.	Is the improvement in extravasation of AP-1-Lipo-DOX related to	(45)

model (NOD-scid Mice)	(AP-1-Lipo-DOX) (Chemotherapy)		Due to labeling of Lipo-Dox before Dox release the Coefficient of Determination is r^2=1 but after Dox release it is unknown.	conjugated Lipo-Dox		changes in BBB/BTB permeability and/or interstitial transport? Did FUS improve AP-1-Lipo-DOX penetration and change Dox cell uptake?	
Human GBM 8401 model (NOD-scid Mice)	Liposomal doxorubicin (Lipo-DOX); AP-1 targeted - Liposomal doxorubicin (AP1-Lipo-DOX) (Chemotherapy)	100-120 nm	N/A	Fluorometric assay	Repeated FUS exposures after drug administration increased the doxorubicin concentration in the tumor by 4.4-fold and 3.7-fold for untargeted liposomal doxorubicin and AP-1 liposomal doxorubicin, respectively.	Did the repeated exposures change BBB/BTB permeability and/or interstitial transport? Did the repeated exposures improve AP-1-Lipo-DOX penetration and change Dox cell uptake?	(46)
Human GBM 8401 model (NOD-scid Mice)	IL-4 receptor targeted Liposomal doxorubicin (IL-4-Lipo-DOX) (Chemotherapy)	100-120 nm	N/A	Immunostaining of tumor cells with fluorescent imaging of Dox	The tumor Dox concentration was significantly higher in tumors treated with the IL-4-Lipo-DOX and FUS. Modest improvement in survival (IST median 67% vs 44%-IL-4-Lipo-DOX alone).	Is the higher Dox concentration in brain tumors related to changes in BBB/BTB permeability and/or interstitial transport? Did FUS improve AP-1-Lipo-DOX penetration and change cell uptake?	(47)
9L gliosarcoma model (Rat)	Liposomal doxorubicin (Lipo-DOX) (Chemotherapy)	90 nm	Contrast-enhanced T1-W MRI. The correlation was not estimated.	Indirect via contrast-enhanced T1-weighted MR images	Multiple treatments with liposomal doxorubicin and ultrasound improved outcomes (IST median 100% vs 16%-Lipo-DOX alone).	Is the improved survival related to higher Dox uptake by cancer cells Did FUS improve Lipo-DOX penetration?	(48)
9L gliosarcoma model (Rat)	Liposomal doxorubicin (Lipo-DOX) (Chemotherapy)	90 nm	Contrast-enhanced T1-W MRI. The correlation was not estimated.	Fluorometric assay	Increased extravasation of lipo-dox when it was administered before sonication (7-fold vs 5-fold improvement as	Is the increased extravasation of Lipo-dox related to changes in BBB/BTB permeability, and/or interstitial transport	(49)

				compared to Lipo-Dox alone).	and/or endothelial cell uptake from to bubble activity? Did FUS improve Lipo-DOX penetration and change Dox cell uptake?	
F98 glioma model (Rats)	Liposomal doxorubicin (Doxil) (Chemotherapy)	90 nm	Contrast-enhanced T1-W MRI. The Coefficient of Determination of Trypan Blue and Dox is r^2=0.97	Fluorometric assay	The use of controlled sonication improved the maximum concentration level of delivered doxorubicin (10μg/mL, >10-fold improvement as compared to drug only)	Did the controller result in optimum BBB/BTB permeability or improved interstitial transport? Did the controller result in improved Doxil penetration and/or change Dox cell uptake?	(50)
9L gliosarcoma and F98 glioma models (Rats)	Cisplatin in Brain-Penetrating Nanoparticles (Chemotherapy)	60 nm	Contrast-enhanced T1-W MRI; Confocal microscopy of florescent labeled particles. Due to labeling of BPN before Cisplatin release the correlation is r^2=1, but after cisplatin release it is unknown.	Confocal microscopy of florescent labeled particles extravasation in brain tumors	28-fold improvement in extravasation in the glioma model. No improvement in survival in FUS treated vs BPN alone animals	Is the increased extravasation of Nanoparticles related to changes in BBB/BTB permeability and/or interstitial transport and/or cell uptake/kinetics? Did FUS improve the Nanoparticle penetration and change cisplatin cell uptake?	(51)
U87 MG glioblastoma model (Mice)	Paclitaxel liposomes (PTX-LIPO) (Chemotherapy)	~90 nm	Evans Blue (4hrs post treatment) and Fluorometric imaging of fluorescent tagged liposomes. Due to labeling of PTX-Lipo before Paclitaxel release, the correlation is r^2=1, but after Paclitaxel release it is unknown.	Fluorometric imaging of liposome and HPLC (PTX)	2-fold increase in the FUS targeted region (3hrs post treatment). Modest but significant improvement in survival (IST median 21% vs 5% - PTX-Lipo alone).	Is the increase of PTX-LIPO in the brain related to changes in BBB/BTB permeability, interstitial transport, and/or cell kinetics for the exposures tested? Did FUS improve PTX-LIPO penetration and change paclitaxel cell uptake)?	(52)

9L gliosarcoma model (Rat)	Liposomal doxorubicin (Lipo-DOX) (Chemotherapy)	90 nm	Dynamic Contrast Enhanced MRI. The correlation was not estimated.	Fluorometric assay	>2-fold increase on Dox concentrations in tumors regardless of the stage of tumor growth. The transfer coefficient K_{trans} for Gd-DTPA in tumors was significantly different from control at small tumor sizes (day 9).	Why the Dox uptake is higher in the sonicated tumors after day 14 and 17 but not the K_{trans}? Did FUS improve Lipo-DOX penetration and change Dox cell uptake?	(53)
C6 glioma model (Rat)	Cilengitide (CGT) (Peptide)	588.67 g/mol	Contrast-enhanced T1-W MR. The correlation was not estimated.	Indirect via contrast-enhanced T1-weighted MR images	Significantly higher apoptotic and autophagy activities were induced by the combined therapy. Modest increase in survival (41.1 ± 2.0 vs 35.0 ± 1.8 days).	Is the increase apoptosis and autophagy in the brain related to improved peptide penetration and CGT and changes in cell uptake?	(54)
9L gliosarcoma model (Rat)	αEGFR-SERS440 Gold Nanoparticles (GNPs)	50-120 nm (PEG-coated)	Contrast-enhanced T1-W MR; Evans Blue; Raman Spectroscopy. The correlation was not estimated.	Raman Spectroscopy	Delivery of SERS 50 or 120 nm gold nanoparticles to the tumor margins (no *in vivo* statistics were provided)	Is the increased delivery of GNPs related to changes in BBB/BTB permeability and/or interstitial transport and/or cell uptake/kinetics? What was the GNPs penetration and cell uptake?	(55)
C6 glioma model (Rat)	Folate-conjugated Polymersomal Doxorubicin (FPD)		T2*-W MRI of SPION nanoparticles; Confocal microscopy. The correlation was not estimated.	HPLC	5.1-fold higher intratumoral Dox than FDP alone. Significant but modest improvement in survival (median survival: 44 days for FDP w FUS vs 29 days for FPD alone.	Is the increased delivery of Dox related to changes in BBB/BTB permeability and/or interstitial transport and/or cell uptake/kinetics? What was the FPD penetration?	(56)

Drug Attached to Magnetic Nanoparticles (MNPs) [b]							
C6 glioma model (Rat)	BCNU - MNP (Chemotherapy)	~10–20 nm	Contrast-enhanced T1-W and T2*-W MRI. Due to labeling of BPN before Cisplatin release the correlation is r^2=1, but after BCNU release it is unknown.	T2*-weighted MR images	T2*W images showed increased uptake of MPs. Significant improvement in survival (no IST median values were provided).	How the magnetic targeting changes the interstitial kinetics? What fraction of the increased uptake of BCNU – MNP is related to FUS-mediated changes in BBB/BTB permeability and/or intestinal transport? Was there an increase in the MNP penetration and change in cell uptake with and without magnetic targeting?	(57)
C6 glioma model (Rat)	Epirubicin - MNP (Chemotherapy)	~12 nm	MRI - R2 map of magnetic particles. Correlation of ΔR2 value and Epirubicin deposition: r^2=0.9.	HPLC	2.6-fold increase in MNP in the brain in the combined treatment (FUS w MT) vs control (FUS w/o MT).	How magnetic targeting changes the interstitial kinetics? Was there an increase in the MNP penetration and change in cell uptake with and without magnetic targeting?	(58)
C6 glioma model (Rat)	Doxorubicin – SPIO (Chemotherapy)	~36 nm (SPIO); ~3 µm; (MBs)	MRI - R2 map of magnetic particles. Correlation of ΔR2 value and SPIO deposition: r^2=0.83; correlation of Dox deposition and SPIO deposition: r^2=0.79.	HPLC	2-fold (HPLC) of Dox increase using magnetic targeting of the SPIO-Dox-microbubble complex (compared to Magnetic targeting and no FUS).	How magnetic targeting changes the interstitial kinetics? Was there an increase in the SPIO penetration and change in Dox cell uptake with and without magnetic targeting?	(59)
Drug Loaded to Microbubbles (MBs)[c]							
C6 glioma model (Rat)	BCNU (Chemotherapy)	214 Da (BCNU); ~1 µm (MBs)	Evans Blue. The correlation was not estimated	HPLC	8-fold increase in BCNU tumor deposition 10 mins post treatment, but marginal deposition at 30 mins (**healthy Brains**).	How the ultrasonic actuation changes the interstitial kinetics? What was the increase in uptake in brain tumors?	(60)

					12% increase in median survival compared to free BCNU.	Was there any improvement in BCNU penetration and change in cell uptake in brain tumors? Was the anti-tumor effect mediated by BCNU or did FUS have a direct cytotoxic effect?	
C6 glioma model (Rat)	BCNU (Chemotherapy)	214 Da (BCNU); ~1 µm (MBs)	Evans Blue; Acoustic Emissions. The correlation between Acoustic emissions change and BCNU in **healthy brain** r^2=96.	HPLC	5.8-fold increase in BCNU accumulation in **healthy brains**. Significant improvement in survival (IST median 52.8% vs 22%-BCNU alone).	How the ultrasonic actuation changes the interstitial kinetics? What was the increase in uptake in brain tumors? Was there any improvement in BCNU penetration and change in cell uptake in brain tumors?	(61)
C6 glioma model (Rat)	VEGFR2-BCNU (Antiangiogenic-targeting with Chemotherapy)	214 Da (BCNU); ~1.8 µm (MBs)	Evans Blue. The correlation was not estimated.	HPLC	1.86-fold increase in BCNU accumulation in **healthy brains.** Significant improvement in survival (IST median 121% vs 37%-VEGFR2 alone).	How the ultrasonic actuation changes the interstitial transport? What was the increase in uptake in brain tumors? Was there any improvement in BCNU penetration and change in cell uptake in brain tumors? Was the anti-tumor effect mediated by VEGFR2-BCNU or did FUS have a direct cytotoxic effect?	(62)

C6 glioma model (Rat)	Folate-conjugated DNA-loaded cationic MBs (FCMBs)	5.5 MDa (152 kbp); 1.1 µm (MBs)	Evans Blue and Fluorescent microscopy of MBs vesicles and IVIS imaging of G-Luc transfection. The correlation was not estimated.	IVIS imaging of G-Luc transfection	4.7-fold improvement in gene transfection efficiency as compared to direct injection at 24hrs. Modest difference at 3 days.	Was there any improvement in DNA penetration and change in cell uptake? How ultrasonic actuation enhanced transfection efficiency?	(63)
C6 glioma model (Rat)	Doxorubicin – SPIO (Chemotherapy)	~36 nm (SPIO); ~1 µm (MBs)	Evans Blue and susceptibility weighted (SWI) MRI. The correlation was not estimated.	Fluorometric assay	1.6-fold increase in SPIO-Dox+FUS uptake comparted to SPIO-Dox alone.	How the ultrasonic actuation and magnetic targeting changes the interstitial kinetics? Was there any improvement in SPIO penetration and change Dox in cell uptake?	(64)

[a] All models are orthotropic; [b] Magnetic actuation of the drug into the tumor interstitial space after FUS-BBB/BTB disruption; [c] The drug might have been propelled into the tumor by the microbubble collapse after the application of FUS. Review Criteria: Information for the data in Table I was compiled by searching the PubMed and Web of Science databases for articles published before March 1st 2018, including early-release publications. Search terms included “focused ultrasound brain tumor”, “ultrasound blood tumor barrier disruption”, “ultrasound blood tumor barrier disruption”, “focused ultrasound blood brain barrier glioma”, and “focused ultrasound blood tumor barrier glioma”. Full articles were checked for additional material when appropriate, and articles that cite key publications were checked.

Table S2. Notations

Symbol	Description
V_{rbc}	RBC velocity in tumor vessels
PV	Vascular outlet pressure
PA	Vascular inlet pressure
PI	Interstitial pressure
μ	Blood viscosity
d	Vessel wall thickness
D_v	Vessel effective diffusion coefficient
D_i	Interstitium effective diffusion coefficient
D_b	Diffusion coefficient in blood
K	Hydraulic conductivity
ε_i	Interstitium porosity
ε_v	Vessel wall porosity
V	Rate of transmembrane transport of doxorubicin
V_b	Rate of doxorubicin binding to nucleus
K_e	Michaelis-Menten kinetics constants
K_i	
k_{on}	T-DM1 Association rate
k_{int}	T-DM1 Internalization constant
k_{off}	T-DM1 Dissociation rate
C_r	Concentration of cell surface receptors
C_e	Extracellular drug concentration
C_i	Intracellular drug concentration
C_b	Bound drug concentration
C_v	Drug concentration inside vessel
J_f	Rate of transvascular fluid flow
J_s	Rate of drug transvascular transport
L_p	Hydraulic conductivity (Darcy's law)
P	Vascular diffusive permeability
σ_f	Reflection coefficient
H	Diffusive hindrance factor
W	Convective hindrance factor
α	the particle size to pore size ratio
P_e	Péclet number
R	Rate of BBB closure
C_{ε_v}	BBB closure constant
C_{D_v}	Doxorubicin BBB closure constant
B_{ε_v}	BBB closure baseline value
B_{D_v}	Doxorubicin BBB closure baseline value

Table S3. Doxorubicin model parameters

Symbol	Value	Units	Description	Reference
V_{rbc}	0.12	mm/s	RBC velocity in tumor vessels	(8)
PV	5	mmHg	Vascular pressure	(6)
PI	1	mmHg	Interstitial pressure	-
μ	0.004	Pa*s	Blood viscosity	(6, 10, 65)
ε_i	0.4	-	Interstitium porosity	(65–68)
ε_v	0.5	-	Vessel wall porosity	-
K	4×10^{-8}	$cm^2/(mmHg*s)$	Hydraulic conductivity	(69)
d	5	μm	Vessel wall thickness	(6)
D_v	1.25	$\mu m^2/sec$	Vessel effective diffusion coefficient	(10, 70)
D_i	40	$\mu m^2/sec$	Interstitium effective diffusion coefficient (Free dox)	(10, 65, 71)
D_b	1×10^{5}	$\mu m^2/sec$	Diffusion coefficient in blood	(72)
V	42.9	nM/s	Rate of transmembrane transport	(73–75)
V_b	0.0016	1/s	Rate of drug binding to nucleus	
K_e	403	nM	Michaelis-Menten kinetics constants	
K_i	63	μM		

Table S4. T-DM1 model parameters.

Symbol	Value	Units	Description	Reference
K	4×10^{-8}	$cm^2/(mmHg.s)$	Hydraulic conductivity	(69)
D_v	4.67×10^{-3}	$\mu m^2/sec$	Vessel effective diffusion coefficient	(10, 70, 76)
D_i	10	$\mu m^2/sec$	Interstitium effective diffusion coefficient	(10)
k_{on}	1.5×10^{4}	$m^2/(sec*mol)$	Association rate	(6, 11, 77)
k_{int}	5×10^{-5}	1/s	Internalization constant	
k_{off}	8×10^{-3}	1/s	Dissociation rate	
C_r	1×10^{-5}	M	Concentration of cell surface receptors	

Table S5. Vascular network model parameters.

Symbol	Value	Units	Description	Reference
PV	5	mmHg	Vascular outlet pressure	(6, 19)
PA	25	mmHg	Vascular inlet pressure	(19)
R	9×10^{-5}	1/s	Rate of BBB closure	(21)
C_{ε_v}	0.34± 0.09	-	BBB closure constant	
C_{D_v}	$1.1\times10^{-12}\pm 1.5\times10^{-13}$	m^2/s	Doxorubicin BBB closure constant	
B_{ε_v}	0.28 ± 0.11		BBB closure baseline value	
B_{D_v}	$3.1\times10^{-13}\pm 1.5\times10^{-13}$	m^2/s	Doxorubicin BBB closure baseline value	